

Numerical Simulation of Three-Dimensional Dendritic Growth

Alain Karma and Wouter-Jan Rappel

*Department of Physics and Center for Interdisciplinary Research on Complex Systems,
Northeastern University, Boston, Massachusetts 02115*

(Received 27 June 1996)

Dendritic crystal growth in a pure undercooled melt is simulated quantitatively in three dimensions using a phase-field approach. The classic parameter σ^* that characterizes the dynamically selected operating state of the dendrite tip as well as the full nonaxisymmetric tip morphology are determined as a function of anisotropy for a crystal with a cubic symmetry. Results are compared to experiment and used to critically test solvability theory. [S0031-9007(96)01568-2]

PACS numbers: 68.70.+w

Dendritic growth has been a central problem in pattern formation [1] and metallurgy [2] for many years. Considerable theoretical progress has been achieved which has led to the development of solvability theory to determine the steady-state operating state of the dendrite tip (i.e., tip velocity V and tip radius ρ) [1,3–8].

Paradoxically, our understanding of pattern selection in three dimensions (3D) has remained uncertain, especially with regard to experiment. This is due to the fact that it has so far remained too difficult to simulate reliably the equations of dendritic growth in 3D even on current supercomputers. This, in turn, has prevented the following: (i) to test whether the global attractor of the growth dynamics is indeed the steady-state needle crystal predicted by solvability theory, and (ii) to test the predictions of this theory which are themselves only approximate in 3D [6–8]. Consequently, it has remained unclear whether existing disagreements between solvability theory and experiment [9–11] are due to the inapplicability of this theory, to the approximate nature of its predictions in 3D, or to some missing physics in the starting equations.

Here we report the results of 3D simulations of dendritic growth in a pure undercooled melt. These simulations are made possible by using a recently developed phase-field approach which renders fully quantitative 3D computations accessible for the first time [12]. This approach also makes it possible to model the experimentally relevant low velocity limit, where the solid-liquid interface can be assumed to relax instantaneously to local thermodynamic equilibrium (i.e., where kinetic effects at the interface are negligibly small). Our numerical results are applied to critically test the applicability of solvability theory in 3D, to make comparison with experiment, and to characterize the full 3D dendrite tip morphology.

The equations of the 3D free-boundary problem are given by

$$\partial_t T = D \nabla^2 T, \quad (1)$$

$$L v_n = c_p D (\partial_n T|_S - \partial_n T|_L), \quad (2)$$

$$T_I - T_M = -\frac{T_M}{L} \sum_{i=1}^2 \left[\gamma(\mathbf{n}) + \frac{\partial^2 \gamma(\mathbf{n})}{\partial \theta_i^2} \right] \frac{1}{R_i}, \quad (3)$$

where T is the temperature field, T_I is the interface temperature, T_M is the melting temperature, D is the diffusivity, L is the latent heat of melting, c_p is the specific heat, v_n is the normal velocity of the interface, and

$$\gamma(\mathbf{n}) = \gamma_0 (1 - 3\epsilon_4) \left[1 + \frac{4\epsilon_4}{1 - 3\epsilon_4} (n_x^4 + n_y^4 + n_z^4) \right] \quad (4)$$

is the surface energy for a crystal chosen to have a cubic symmetry. In addition, θ_i are the angles between the normal \mathbf{n} and the two local principal directions on the boundary, and R_i are the principal radii of curvature. Growth is controlled by the undercooling $\Delta = (T_M - T_\infty)/(L/c_p)$ where T_∞ is the initial melt temperature.

We use three key ingredients to solve the above equations. Firstly, we avoid the usual difficulties of tracking a sharp boundary by using a phase-field approach [13–17]. In this approach, the two-phase system is described by a phenomenological free energy

$$\mathcal{F} = \int d\mathbf{r} [W^2(\mathbf{n}) |\nabla \psi|^2 + f(\psi, u)], \quad (5)$$

where $u \equiv (T - T_M)/(L/c_p)$ is the dimensionless temperature field. We have used here the form $f(\psi, u) = -\psi^2/2 + \psi^4/4 + \lambda u \psi (1 - 2\psi^2/3 + \psi^4/5)$ with minima at $\psi = -1$ and $\psi = +1$ which correspond to the liquid and solid phases, respectively. The anisotropic surface energy defined by Eq. (4) is recovered by choosing $W(\mathbf{n}) = W_0 \gamma(\mathbf{n})/\gamma_0$, with $\mathbf{n} \equiv \nabla \psi / |\nabla \psi|$, which is the direct 3D generalization of the way anisotropy has been previously included in two dimensions (2D) [15–18]. The phase field ψ varies between its two minima values across an interfacial region of width W_0 , thereby distinguishing between phases without front tracking. It obeys the first order kinetic equation

$$\tau(\mathbf{n}) \frac{\partial \psi}{\partial t} = -\frac{\delta \mathcal{F}}{\delta \psi}, \quad (6)$$

and is coupled to the diffusion equation

$$\frac{\partial u}{\partial t} - \psi \partial t \quad (7)$$

for the temperature field with an added source term that represents the simplest phenomenological way of including the generation of latent heat at the interface [12–15]. These equations reduce to those of the original solidification equations in the sharp-interface limit, where W_0 is small compared to the principal radii of curvature of the boundary.

Secondly, and most importantly, we exploit the results of a recent analysis [12] to relate the phase-field model parameters to those of the sharp-interface equations. As demonstrated in 2D [12], this analysis makes it possible (i) to perform computations with a smaller capillary length, $d_0 = \gamma_0 T_M c_p / L^2$, and (ii) to choose λ and the function $\tau(\mathbf{n})$ in such a way that we obtain a Gibbs-Thomson condition without interface kinetics in the sharp-interface limit [12]. That is we recover exactly Eq. (3) without an additional velocity-dependent term in this limit. Since the computation time scales as $(d_0/W_0)^5$ in 3D, this first property dramatically enhances the computational efficiency of the phase-field approach and allows us to model dendritic growth quantitatively, as opposed to nonquantitatively in 3D as previously [15]. Furthermore, it permits us to model an undercooling range, where the dendrite tip Péclet number $P \equiv \rho V / 2D$ is small enough to compare $\sigma^* \equiv 2Dd_0/\rho^2 V$ to its measured small undercooling values [9,10].

Lastly, we are able to resolve numerically very small anisotropies by incorporating quantitatively the contribution of the grid anisotropy. For a given value of ϵ_4 used in $W(\mathbf{n})$, we compute the equilibrium shape produced by the phase-field model. The grid-corrected anisotropy is then defined as that value of ϵ_4 in $\gamma(\mathbf{n})$ which produces a 3D equilibrium shape that matches exactly that of the phase-field model. A procedure that will be described elsewhere was also developed to obtain a grid-corrected $\tau(\mathbf{n})$. Numerical tests were performed in 2D to check that this procedure yields accurate values of σ^* over the entire range of ϵ_4 investigated here in 3D.

Equations (6) and (7) were simulated explicitly with a grid spacing ranging between 0.6 and 0.8 with $W_0 = 1$, D ranging between 0.5 and 4, a time step ranging between 0.01 and 0.08, and a constant undercooling $\Delta = 0.45$. The anisotropy was varied from $\epsilon_4 = 0.0066$ to $\epsilon_4 = 0.047$ which spans most of the range of experimental interest. Figure 1 shows a typical 3D dendrite morphology resulting from the growth of a small spherical seed. Quantitative results which pertain to the steady-state operating state and morphology of the dendrite tip are presented in Table I and Figs. 2 and 3. These were obtained with long simulations that focused on the steady-state growth of a single dendrite tip along the z axis. Several runs were performed to check that the values in Table I are independent of d_0/W_0 within an accuracy of 10%.

In order to test solvability theory, we have computed independently the values of P and σ^* predicted by the numerical solution of the steady-state growth equations



FIG. 1. Result of a 3D phase-field simulation on a $300 \times 300 \times 300$ cubic lattice for $\epsilon_4 = 0.047$ which shows dendrite tips growing along the principal $\langle 100 \rangle$ directions. The simulation was performed in the first octant ($x, y, z \geq 0$) with a spherical nucleus centered at the origin as the initial condition. The solid-liquid boundary shown here corresponds to the $\psi = 0$ surface reconstructed by reflection about the $x = y = z = 0$ planes. The structure is seen from an angle where all six $\langle 100 \rangle$ directions are visible.

using the standard axisymmetric approximation, where the surface energy and steady-state shape are assumed to be independent of the polar angle ϕ in the x - y plane perpendicular to the growth axis [6]. This is the same calculation performed by Kessler and Levine in Ref. [6], and we have checked that our boundary integral code reproduces their results within 1%. For completeness, we also report the predictions of the linear solvability theory of Barbieri and Langer [7] which uses a shape linearized around the Ivantsov paraboloid of revolution [19] and the same axisymmetric approximation.

TABLE I. Result of phase-field simulations on a $200 \times 200 \times 400$ cubic lattice compared to the results of the numerical and linear solvability theories for $\Delta = 0.45$. A and α characterize the amplitude of the fourfold symmetry component of the tip morphology in simulations. Typical runs took 60–140 CPU hours on a DEC-ALPHA 3000-700 work station, and shorter times on a CRAY-YMP and a CRAY-T3D.

ϵ_4	Phase-field simulations				Solvability theory			
	P	σ^*	α	A^{-1}	Numerical P	Numerical σ^*	Linear P_{lv}	Linear σ^*
0.0066	0.426	0.015	1.78	13.0	0.418	0.0128	0.471	0.0116
0.0123	0.360	0.036	1.73	11.3	0.367	0.0329	0.471	0.0250
0.0171	0.312	0.063	1.68	10.1	0.324	0.0578	0.471	0.0367
0.0265	0.236	0.16	1.62	7.8	0.247	0.142	0.471	0.0602
0.0369	0.159	0.47	1.57	5.7	0.172	0.365	0.471	0.0890
0.0470	0.093	1.72	1.54	4.0	0.109	1.037	0.471	0.1240

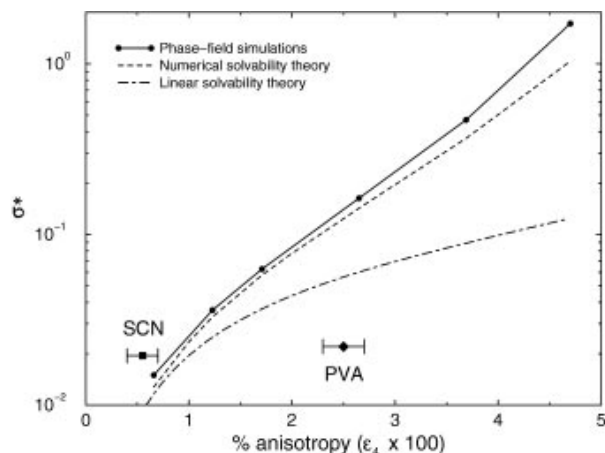


FIG. 2. Plot of σ^* vs ϵ_4 for $\Delta = 0.45$ showing the results of phase-field simulations compared to the approximate predictions of the numerical and linear solvability theories. Also plotted are the small Δ experimental values of σ^* for SCN [9] and PVA [10], using the ϵ_4 measurements of Ref. [11].

As shown in Table I, the numerical solvability theory yields σ^* values which are systematically lower than the phase-field results, but still reasonably close for small anisotropy. The predicted values of σ^* , however, start to become significantly inaccurate for anisotropies greater than about 3%, although predictions of the Péclet number remain relatively accurate. Most likely, this does not indicate a breakdown of solvability theory, but of the axisymmetric approximation. This conclusion is supported by the fact that the fourfold deviation from a shape of revolution increases in magnitude with anisotropy (as described below) and, hence, can affect the selection. It is also supported by the fact that we do not observe any sidebranching [1,9,20] without adding noise to the phase-field equations. Hence, our simulations rule out the possibility of a dynamical attractor other than a steady-state needle crystal. The linear theory is seen to break down at much smaller anisotropy. This is because it assumes that the steady-state shape remains close to the Ivantsov paraboloid of revolution. Table I shows that the actual Péclet number already starts deviating significantly from its Ivantsov value, P_{1V} [19], at small anisotropy.

The steady-state morphology of the dendrite tip was analyzed using the Fourier decomposition

$$r^2(\phi, z) = \sum_n A_n(z) \cos 4n\phi, \quad (8)$$

where r is the radial distance from the z axis. Both r and z are measured in units of ρ with the tip at $z = 0$. This decomposition has the advantage that it is general and does not presuppose a particular analytical form to fit the tip shape. The function $A_0(z)$ is the axisymmetric contribution to this shape. It approaches a paraboloid of revolution, $A_0(z) = -2z$, for small $|z|$ and departs from this shape with increasing $|z|$ as shown in Fig. 3, this departure being more pronounced at larger

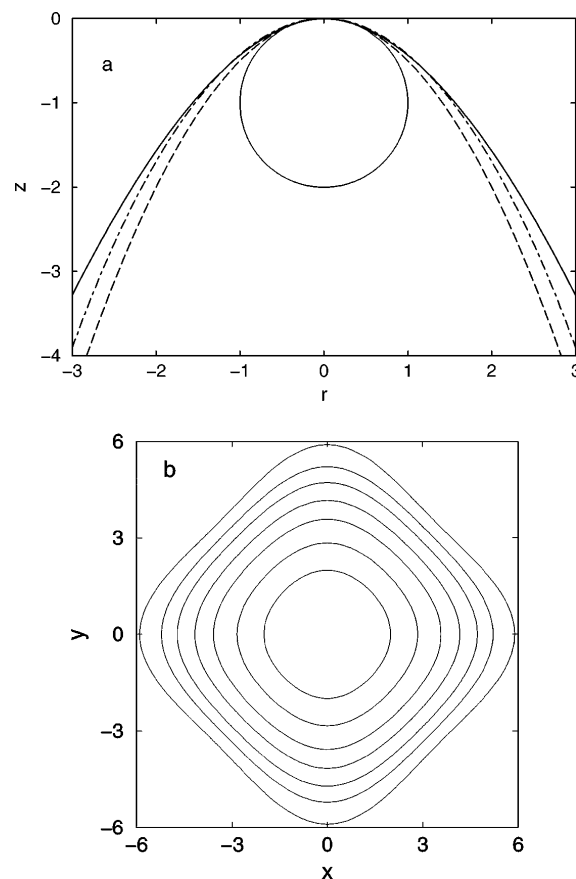


FIG. 3. Steady-state tip morphology for $\epsilon_4 = 0.0123$ shown in (a) the $\phi = 0^\circ$ (solid line) and $\phi = 45^\circ$ (dash-dotted line) planes, and (b) (100) planes equally spaced along z by one tip radius. The length is measured in units of ρ . The Ivantsov parabola $z = -r^2/2$ (dashed line) and a circle of unit radius are superimposed in (a). The Fourier amplitudes at two tip radii behind the tip in (b) are $A_1(-2) = 0.29$, $A_2(-2) = 0.020$, and $A_3(-2) = 0.0022$, illustrating that the tip morphology is dominated by the fourfold symmetry mode.

anisotropy as one would expect. More important is the nonaxisymmetric departure from this shape of revolution which is contained in the higher modes, $A_n(z)$ for $n \geq 1$. The amplitude of the first fourfold symmetry mode turns out to be much larger than all the other modes (Fig. 3) and to be well described by the power law $A_1(z) = A|z|^\alpha$, which appears as a straight line on a log-log plot of $A_1(z)$ vs $|z|$ for $|z|$ varying between approximately $\rho/10$ and 5ρ [21]. Furthermore, the values of A and α in Table I clearly show that the amplitude of the fourfold symmetry mode is sensitively dependent on anisotropy which is a qualitatively novel aspect of our results. The linear solvability calculation of Ben-Amar and Brener [8] had previously predicted that the tip morphology should be independent of anisotropy for asymptotically small anisotropy, with $A^{-1} = 11$ and $\alpha = 2$ for small $|z|$. The values of A and α listed in Table I indicate that the range of small anisotropy, where this prediction is likely to be valid, lies outside the range simulated here. This is also

consistent with the fact that their calculation is only valid in the limit where $\sigma^* \sim \epsilon_4^{7/4}$, and that this 7/4 power law scaling is not yet attained at the smallest computed anisotropy in Fig. 2.

For $\epsilon_4 = 0.0066$, which lies inside the range of uncertainty of the measured value $\epsilon_4 = 0.0055 \pm 0.0015$ for SCN [11], our simulations yield a value of $\sigma^* \approx 0.015$ with $P = 0.426$. This value is only 20% smaller than the value $\sigma^* = 0.0192$ measured by Huang and Glicksman [9] for this material. Most of this discrepancy can be accounted for by the finite Péclet number correction which can be estimated, using the numerical solvability code, to decrease σ^* by about 15% from its zero Péclet number limiting value. Therefore we obtain a reasonably good agreement with experiment for SCN within the existing uncertainty in the measured value of anisotropy. Pivalic acid (PVA) [10], however, remains problematic as seen in Fig. 2, and a closer examination of kinetic effects for this material could potentially resolve this large discrepancy. Finally, Maurer, Perrin, and Tabeling [22] have found that the tip morphology of NH_4Br dendrites is indeed well described by a single $\cos 4\phi$ mode, while LaCombe *et al.* have found that, for SCN dendrites, more modes seem necessary to fit the tip morphology [23]. The origin of this difference, which is potentially due to noise amplification, also remains to be understood.

In conclusion, we have demonstrated that quantitative modeling of 3D dendritic growth is possible using a recently developed phase-field methodology [12]. Our results are important in that they leave little doubt about the conceptual validity of solvability theory in 3D and the importance of crystalline anisotropy, and yield results which are consistent with experiment, at least for SCN where kinetic effects are believed to be small. At present, the applicability of solvability theory—in terms of making accurate predictions—remains limited mainly by the axisymmetric approximation at large anisotropy. Our results have shown that the three-dimensional morphology of the dendrite tip is dominated by a fourfold component whose amplitude depends sensitively on anisotropy. This prediction should be testable experimentally. A host of other microstructural pattern formation issues, such as the determination of the steady-state shape further behind the tip and sidebranching, are now amenable to quantitative study using the present computational approach.

This research was supported by a DOE grant and benefited from supercomputer time allocation at NERSC. We thank Stuart Levy of the Geometry Center at the

University of Minnesota for his help in visualizing our results and Martine Ben-Amar for useful exchanges.

-
- [1] J.S. Langer, in *Chance and Matter*, edited by J. Souletie, J. Vannimenus, and R. Stora, Lectures on the Theory of Pattern Formation, Les Houches, Session XLVI (North-Holland, Amsterdam, 1987), pp. 629–711; D. Kessler, J. Koplik, and H. Levine, *Adv. Phys.* **37**, 255 (1988).
 - [2] W. Kurz and D.J. Fisher, *Fundamentals of Solidification* (Trans Tech, Switzerland, 1989).
 - [3] D.A. Kessler, J. Koplik, and H. Levine, *Phys. Rev. A* **31**, 1712 (1985).
 - [4] E. Ben-Jacob, N.D. Goldenfeld, B.G. Kotliar, and J.S. Langer, *Phys. Rev. Lett.* **53**, 2110 (1984).
 - [5] J.S. Langer, *Phys. Rev. A* **33**, 435 (1986).
 - [6] D.A. Kessler and H. Levine, *Acta Metall.* **36**, 2693 (1988).
 - [7] A. Barbieri and J.S. Langer, *Phys. Rev. A* **39**, 5314 (1989).
 - [8] M. Ben-Amar and E. Brener, *Phys. Rev. Lett.* **71**, 589 (1993).
 - [9] S-C. Huang and M.E. Glicksman, *Acta Metall.* **29**, 701 (1981).
 - [10] M.E. Glicksman and N.B. Singh, *J. Cryst. Growth* **98**, 277 (1989).
 - [11] M. Muschol, D. Liu, and H.Z. Cummins, *Phys. Rev. A* **46**, 1038 (1992).
 - [12] A. Karma and W.J. Rappel, *Phys. Rev. E* **53**, R3017 (1996).
 - [13] J.S. Langer, *Directions in Condensed Matter* (World Scientific, Singapore, 1986), p. 164.
 - [14] J.B. Collins and H. Levine, *Phys. Rev. B* **31**, 6119 (1985).
 - [15] R. Kobayashi, *Physica (Amsterdam)* **63D**, 410 (1993).
 - [16] A.A. Wheeler, B.T. Murray, and R. Schaefer, *Physica (Amsterdam)* **66D**, 243 (1993).
 - [17] S-L. Wang and R.F. Sekerka, *Phys. Rev. E* **53**, 3760 (1996).
 - [18] G.B. McFadden, A.A. Wheeler, R.J. Braun, S.R. Coriell, and R.F. Sekerka, *Phys. Rev. E* **48**, 2016 (1993).
 - [19] G.P. Ivantsov, *Dokl. Akad. Nauk SSSR* **58**, 567 (1947). P_{1v} is defined by $\Delta = P_{1v} \exp(P_{1v}) E_1(P_{1v})$, where $E_1(x)$ is the exponential integral function.
 - [20] A. Dougherty, P.D. Kaplan, and J.P. Gollub, *Phys. Rev. Lett.* **58**, 1652 (1987).
 - [21] Note that the analyticity of the 3D tip shape only requires that $\alpha \rightarrow 2$ in the limit of $|z| \rightarrow 0$.
 - [22] J. Maurer, B. Perrin, and P. Tabeling, *Europhys. Lett.* **14**, 575–579 (1991).
 - [23] J.C. LaCombe, M.B. Koss, V.E. Fradkov, and M.E. Glicksman, *Phys. Rev. E* **52**, 2778 (1995).